ACS APPLIED MATERIALS & INTERFACES

www.acsami.org

Research Article

Scalable Printing of Prussian Blue Analogue@Au Edge-Rich Microcubes as Flexible Biosensing Microchips Performing Ultrasensitive Sucrose Fermentation Monitoring

Ke Zhang, Meiqi Wang, Tao Liu, Zhenyu Chu,* and Wanqin Jin

Cite This: *ACS Appl. Mater. Interfaces* 2022, 14, 40569–40578

Read Online

ACCESS | Metrics & More | Article Recommendations | Supporting Information

ABSTRACT: Sucrose is one of the most applied carbon sources in the fermentation process, and it directly determines the microbial metabolism with its concentration fluctuation. Meanwhile, sucrose also plays a key role of a protective agent in the production of biological vaccines, especially in the new mRNA vaccines for curing COVID-19. However, rapid and precise detection of sucrose is always desired but unrealized in industrial fermentation and synthetic biology research. In order to address the above issue, we proposed an ultrasensitive biosensor microchip achieving accurate sucrose recognition within only 12 s, relying on the construction of a Prussian blue analogue@Au edge-rich (PBA@AuER) microarchitecture. This special geometric structure was formed through exactly inducing the oriented PBA crystallization toward a certain plane to create more regular and continuous edge features. This composite was further transformed to a screen-printed ink to directly and large-scale fabricate an enzymatic biosensor microchip showing ultrahigh sensitivity, a wide detection range, and a low detection limit to the accurate sucrose recognition. As confirmed in a real alcohol fermentation reaction, the as-prepared microchip enabled us to accurately detect the sucrose and glucose concentrations with outstanding reusability (more than 300 times) during the whole process through proposing a novel analytical strategy for the binary mixture substrate system.

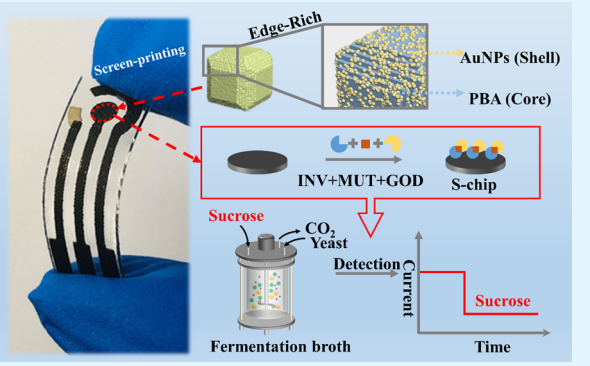

KEYWORDS: *biosensor microchip, edge-rich microarchitecture, fast response, fermentation monitor, ultrasensitive sucrose recognition*

1. INTRODUCTION

Sucrose is widely known as an indispensable sweetener found in breads and beverages in our daily life. Importantly, it is also widely used in industries such as the pharmaceutical industry, microbial industry, and fermentation engineering.[1] Among them, sucrose as a basic substance can be used to produce various products, such as lactic acid, dextran, acetic acid, citric acid, ethanol,[2] and even new biological medicine and vaccines.[3] Pfizer-BioNTech clearly discloses that sucrose is one of the important excipients in the COVID-19 vaccines.[4] Meanwhile, in the Moderna COVID-19 vaccines, sucrose also serves as an essential auxiliary substance to improve the stability of mRNA.[5] However, due to the complex composition of the freeze-dried vaccine, the content of sucrose is likely to have an impact on the efficacy of the vaccine itself.[6] Similarly, during the real fermentation processes, the sucrose concentration always determines the reaction efficiency.[7] For instance, in the lactic acid fermentation, when the sucrose substrate concentration is maintained at 50−100 g/L, the maximum lactic acid yield (5.2 g/L/h) is obtained. However, if the sucrose substrate concentration is higher than 150 g/L, the yield of lactic acid will be significantly reduced to 3.0 g/L/h.[8] Therefore, the fast and accurate detection of the sucrose concentration is essential for the precise process control in the synthetic biology research and industrial fermentation.[9] At present, common sucrose detection methods include chromatography, spectrophotometry, qualitative chemical methods, refraction, optical rotation, and so on.[10] These methods are limited due to either requirement of expensive and bulky equipment or certain deficiencies such as time-consuming and complicated operation, which are unable to satisfy both high accuracy and real-time report in the sucrose test.[11,12]

Electrochemical biosensing technology possesses advantages including fast response, high selectivity, and low cost; hence, it has been widely applied in the clinical diagnosis of various physiological indices, such as glucose.[13−15] Nevertheless, because the target concentration in fermentation is much higher than that in body fluids, it is difficult to adopt the

Received: May 26, 2022
Accepted: August 22, 2022
Published: September 1, 2022

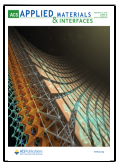

https://doi.org/10.1021/acsami.2c09446
ACS Appl. Mater. Interfaces 2022, 14, 40569−40578

clinical biosensor directly for the test of the fermentation broth.[16,17] Considering that sucrose is hydrolyzed into glucose and fructose by sucrase in the intestinal cavity in the process of human absorption,[18,19] thereby, this metabolic pathway can be adopted to design an enzymatic reaction for the construction of an ultrasensitive and wide-range sucrose biosensor to match the fermentation process. Prussian blue (PB) and its analogues (PBAs) have been proved to possess ultrahigh electrocatalysis and specificity to enzymatic reactions in our previous studies.[20,21] Therefore, we selected the Cu−Co PBA as the core material for the sucrose recognition. However, this PBA is a semiconductor with a wide band gap (~1.84 eV) to present a poor conductivity, which may greatly reduce the strength of the response current. In this case, we introduced gold nanoparticles (AuNPs) as the shell to eliminate this deficiency. The coupling of AuNPs could play the role of current signal amplification, which effectively optimized the deficiency of poor conductivity in PBA. Moreover, due to the loading of AuNPs, the effective catalytic area of the PBA can be increased, so as to form more active sites on the surface of the composite for electrocatalysis. Consequently, we constructed the PBA@Au composite as the biosensing material for detecting sucrose.

In this work, we proposed a fermentation-oriented sucrose biosensor microchip relying on the construction of a Prussian blue analogue@Au edge-rich (PBA@AuER) microcube-based composite material, achieving the accurate and fast detection during the fermentation process. Compared with a common regular cubic morphology, an edge-rich architecture can improve the sensing performance of H_2O_2 by ca. 40%, benefiting from the larger effective catalytic area.[22] As shown in Figure 1, the edge-rich microarchitecture was simply

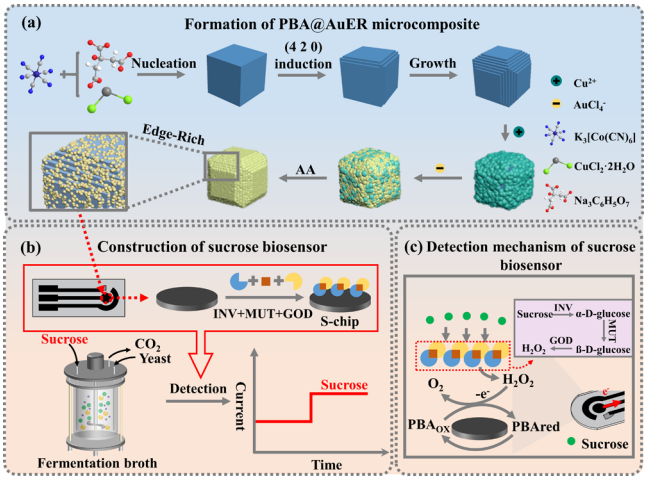

Figure 1. (a) Schematic of the synthesis strategy of the PBA@AuER microcomposite. (b) Construction of the sucrose biosensor; insets: INV: invertase, MUT: mutarotase, GOD: glucose oxidase, and S-chip: sucrose microchip. (c) Detection mechanism of the sucrose biosensor.

prepared by a one-step coprecipitation method of Cu−Co PBA controlled by the sodium citrate complex cations. Then, colloidal Au nanoparticles were thereafter decorated in situ on the edge-rich PBA microcubes to prepare a microcomposite with both high electrocatalysis and conductivity, increasing the detection sensitivity of H_2O_2 by nearly three times. This microcomposite was further transformed into screen-printed ink for large-scale fabrication of biosensor microchips.[23] After the coimmobilization of the three enzymes, only requiring a 12 s response, the as-prepared microchip exhibited a high sensitivity and selectivity for recognizing sucrose among multiple interfering substances with an outstanding reuse stability beyond 300 repetitive detections within 30 days. Moreover, an analytical equation of a binary mixture system containing glucose and sucrose was simulated to match the practical alcohol fermentation process, and its accuracy was confirmed in a real fermentation broth.

2. RESULTS AND DISCUSSION

2.1. Structure Evolution of the PBA@AuER Microcomposite. To synthesize Cu−Co PBA, while using $CuCl_2 \cdot 2H_2O$ and $K_3[Co(CN)_6]$ solutions as the coordination reactants, its morphology is often difficult to control owing to the fast reaction rate causing the insufficient surface growth (Figure S1a). We characterized the Cu−Co PBA prepared at different molar ratios of copper ion over sodium citrate concentrations by field-emission scanning electron microscopy (FESEM) in the Supporting Information (Supplement S1). To slow down this rate, sodium citrate was induced to act as a complexing agent to compete with the coordination reaction between Cu^{2+} and $[Co(CN)_6]^{3-}$ due to its effective chelating ability.[24] In this case, the molar ratio of sodium citrate to Cu^{2+} is the primary parameter for the obtained PBA morphology. We selected three different molar ratios of copper ions to sodium citrate (1:1, 1:1.5, and 1:2) to investigate their effects on PBA morphology. At a 1:1 ratio (Figure S1b), although the synthesized PBA presented a cubic appearance, the crystal size distribution was very wide, ranging from 0.1 to 1 μm. When the added amount of sodium citrate was increased to 1:1.5 (Figure S1c), it was observed that all the prepared crystals possessed a uniform size of ca. 1 μm, which was selected as the optimum condition. However, upon further increasing the sodium citrate ratio to 1:2, rare PBA crystals were obtained even when the reaction time was prolonged to 72 h. This is because all Cu^{2+} ions were coordinated to sodium citrate to block the reaction with $[Co(CN)_6]^{3-}$ ions for PBA synthesis. Moreover, we further studied the influence of Cu^{2+} and $[Co(CN)_6]^{3-}$ concentrations on the PBA structure. As shown in Figure 2a, we synchronously increased the concentration of Cu^{2+} and $[Co(CN)_6]^{3-}$ ions from 20 to 40 mM, revealing the

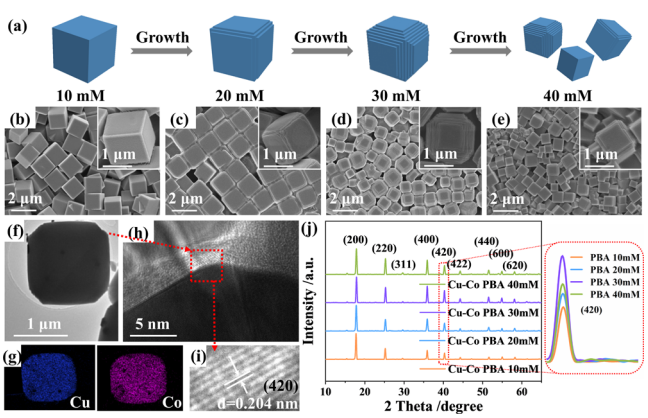

Figure 2. (a) Schematic image of the reaction steps to synthesize PBA. FESEM images of the PBA prepared at different $CuCl_2$ concentrations: (b) 10 mM, (c) 20 mM, (d) 30 mM, and (e) 40 mM. (f) TEM image of the PBAER microcube. (g) EDX mapping results for Cu and Co. (h−i) SAED pattern of the PBAER microcube and the (j) XRD patterns.

https://doi.org/10.1021/acsami.2c09446
ACS Appl. Mater. Interfaces 2022, 14, 40569−40578

feature evolution of PBA, particularly at its edge sites. The FESEM images indicate that more reactants enabled the production of more edges (Figure 2b–d). These edges presented a stacked multilayer structure with the gradually decreasing size (1.20–0.61 μm) from bottom to top to form an edge-rich microcubic shape. Nevertheless, if the added amount of reactants is excessively high, the crystal would repair these incomplete edges, resulting in their return to the cubic shape (Figure 2e). These results confirm that the edge-rich crystal is in a transition state during the formation of PBA microcubes, and sodium citrate is capable of reducing the crystallization rate to reveal the edge-rich appearance. The growth mechanism was further explored using transmission electron microscopy (TEM). We selected a single crystal (Figure 2f) to focus on the edge sites for this study. According to the energy-dispersive X-ray analysis (EDX) mapping results of this crystal (Figure 2g), the copper and cobalt elements were uniformly distributed, proving the successful crystallization of PBA. As observed in Figure 2h,i, the edge exhibited oriented diffraction of the crystal plane with an interplanar spacing of 0.204 nm, which is in agreement with the (4 2 0) plane of the PBA. For more clarity, we tested the X-ray diffraction (XRD) diagrams of the different PBA crystals in Figure 2b–e. The peak representing the (4 2 0) crystal plane first increased when the reactant concentration increased from 10 to 30 mM (Figure 2j). A remarkable improvement in this peak is observed at 30 mM. In contrast, continuing to increase the concentration only caused a decrease in the peak strength. This behavior corresponds well with the number of derivative edges. More edges were generated, and a stronger peak intensity was obtained. Therefore, this evidence has demonstrated that the edge-rich architecture was produced owing to the competition between sodium citrate and $[Co(CN)_6]^{3-}$ during coordination with Cu^{2+}, which induced oriented crystal growth toward the (4 2 0) plane. With the help from both TEM and XRD characterizations, it is proved that the material will produce rich edges when growing along the (4 2 0) crystal plane. Therefore, the growth of Cu–Co PBA toward the (4 2 0) crystal plane can expose more active sites, so that its electrocatalytic ability can be improved, which is more conducive to the realization of high-performance sucrose sensing.

According to the definition of current, its intensity is determined by the electron quantity and transfer time, which are related to the electrocatalysis and conductivity of the electrode material during the electrochemical process.[25] As confirmed in our previous work, PBA often has a high electrocatalytic ability for H_2O_2 reduction but weak conductivity because of its high band gap.[26] Hence, as shown in Figure 1, Au nanoparticles (AuNPs) were induced to decorate the PBA surface to promote conductivity. A chemical reduction method of $HAuCl_4$ was adopted to in situ prepare AuNPs in the water suspension of the obtained edge-rich PBA.[27] After finishing the preparation of PBAER microcubes, extra Cu^{2+} ions were continuously injected into the sky blue suspension of PBA. In this case, some of these positive ions would be attracted on the crystal by their active adsorption sites, which produced a positive surface to benefit the further attraction of $[AuCl_4]^-$ for generating Au nanoparticles. Figure 3a–c indicates that the amount of AuNPs formed remarkably increased with the increasing reactant concentration. However, excess AuNPs caused heavy intergrowth to form a thick layer on the PBA surface, covering the rich edges of the crystal and

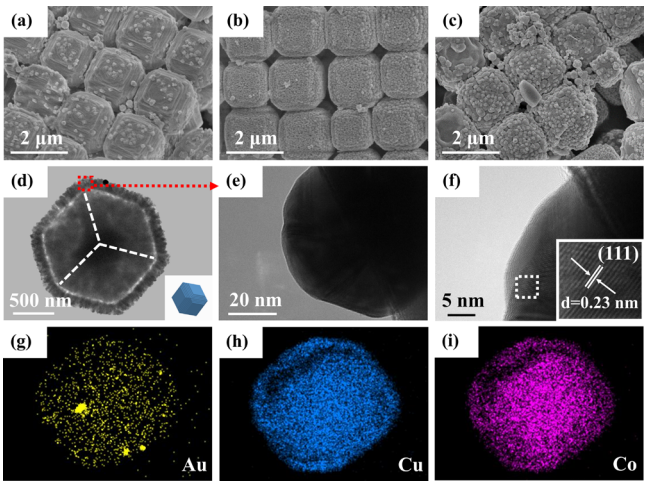

Figure 3. FESEM images of the PBA@AuER microcube prepared by using different $HAuCl_4$ concentrations: (a) 2 mM, (b) 5 mM, and (c) 8 mM. (d) TEM image of the Cu–Co PBA@AuER microcube. (e) TEM image of the AuNPs and (f) SAED pattern of the AuNPs. (g–i) EDX mapping results for Au, Cu, and Co, respectively.

greatly reducing its surface area. Considering the uniform distribution and unchanged crystal structure, the microcomposite in Figure 3b prepared with 5 mM $HAuCl_4$ is the optimum electrode material. This PBA@AuER microcube was composed of a continuous layer with a thickness of ca. 130 nm surrounding the PBA surface (Figure 3d). Each particle of ca. 70 nm was connected to form this shell layer (Figure 3e). The electron diffraction map of the nanoparticles indicated the existence of a typical (1 1 1) plane of Au (Figure 3f), confirming that this particle is the AuNP. In addition, elemental analysis revealed that Cu and Co belonged to the PBA crystal located as the core, which was uniformly covered by Au, and they belonged to the AuNPs as the shell (Figure 3g–i). The chemical composition and elemental valence states of PBA and AuNPs in the composite were analyzed using X-ray photoelectron spectrometry (XPS). (XPS spectra of PBA@AuER microcubes are shown in the Supporting Information (Supplement S2).)

2.2. Electrochemical Behavior of the PBA@AuER Microcube-Based Film. The composites were fixed on the bare gold electrodes for the comparisons of electrochemical behavior. Despite the lack of a bridge force for connection, the PBA@AuER microcubes exhibited excellent electrochemical stability during 30 repetitive cyclic voltammetry (CV) scans (Figure 4a), suggesting the stable structure of this core–shell framework. The reactions that correspond to the redox peaks in Figure 4b have been explained as follows:

$$Cu_3^{(II)}[Co^{(III)}(CN)_6]_2 + 5e^- + 5K^+ \rightarrow K_5Cu_3^{(I)}[Co^{(II)}(CN)_6]_2 \quad (1)$$

$$K_5Cu_3^{(I)}[Co^{(II)}(CN)_6]_2 - 5e^- - 5K^+ \rightarrow Cu_3^{(II)}[Co^{(III)}(CN)_6]_2 \quad (2)$$

As shown in the above equation, the as-prepared PBA undergoes oxidation reaction at a positive potential of ca. +0.3 V (eq 2) and reduction reaction at a negative potential of ca. +0.1 V (eq 1). According to Figure 4b, it can be concluded that the formation of a AuNP layer on the PBA surface was beneficial for both electrocatalysis and electron transfer. For

https://doi.org/10.1021/acsami.2c09446
ACS Appl. Mater. Interfaces 2022, 14, 40569–40578

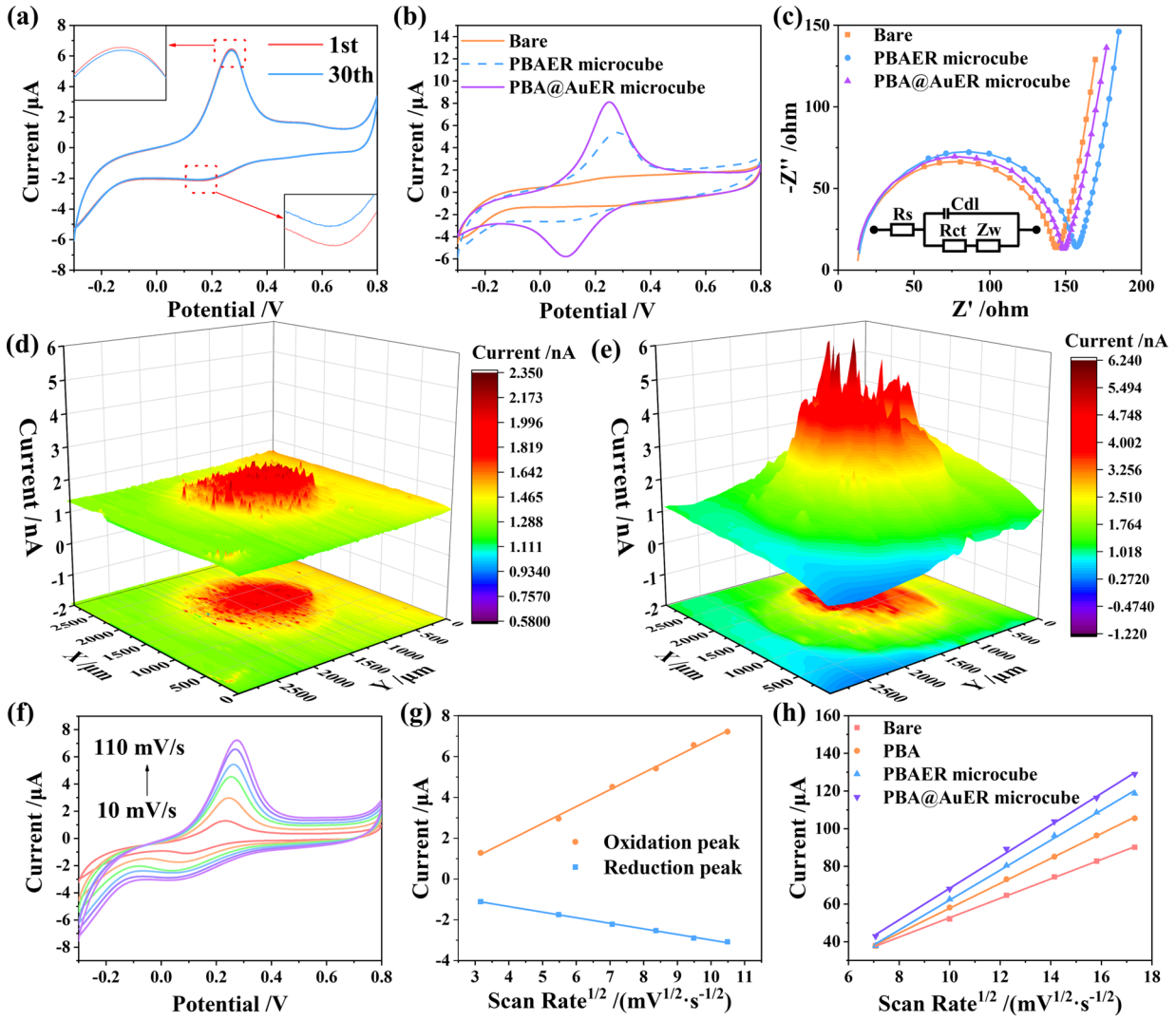

Figure 4. (a) Repetitive CV tests of the prepared sensor for the stability investigation, and the insets show the magnifications of the redox peaks. (b) Comparison of CV values of the bare gold electrode, PBAER microcubes, and PBA@AuER microcube-modified gold electrodes at a scan rate of 0.05 V/s in a 0.05 M PBS. (c) EIS diagrams of the above three electrodes at a scanning frequency range from 0.1 to 100 kHz; inset: electrical equivalent circuit. (d) PBAER microcube SECM catalytic activity scanning. (e) PBA@AuER microcube SECM catalytic activity scanning. (f) CV curve of the PBA@AuER microcube fixed on the gold disk electrode at different scan rates in 0.05 M PBS with 0.1 mM H_2O_2. (g) Calibration curve of the peak current versus the square root of the scan rate for PBA@AuER microcube-modified gold electrodes. (h) Calibration curves of the peak current versus the square root of the scan rate for the bare gold electrode, PBA, PBAER microcubes, and PBA@AuER microcubes.

clarity, the three electrodes were characterized using electrochemical impedance spectroscopy (EIS). EIS scans were taken for each electrode three times. The relative standard deviation (RSD) values for the bare gold electrode and PBAER microcube- and PBA@AuER microcube-modified electrodes were 2.35, 3.21, and 2.46%, respectively. The electron transfer resistances were fitted according to the equivalent circuit shown in Figure 4c, which were calculated to be 102 ± 2, 111 ± 4, and 104 ± 3 Ω for the bare gold electrode, PBAER microcubes, and PBA@AuER microcubes, respectively. This result also proves the promotion of the electron transfer rate derived from the AuNPs. With the aid of a scanning electrochemical microscope (SECM), we can further compare the catalytic activities of the PBAER microcubes (Figure 4d) and PBA@AuER microcubes (Figure 4e). Although the loading of gold nanoparticles effectively enhanced the conductivity of the PBAER microcubes, the response current isosurface of the PBA@AuER microcubes is nearly three times higher than those of the PBAER microcubes. This also means that these composites possess the strongest electrocatalytic activity. Then, the electron transfer mechanism was investigated by CV scanning at different rates ranging from 10 to 110 mV/s in phosphate buffer solution (PBS) with 0.1 mM H_2O_2. As shown in Figure 4f, it is observed that both oxidation and reduction peaks simultaneously increased with the scan rate lifting. After fitting in Figure 4g, the current values belonging to the oxidation and reduction peaks of each scan rate followed a linear relationship with the arithmetic square root of the scan rate. Undoubtedly, the electron transfer process on the film was not controlled by adsorption but was dominated by linear concentration diffusion, which met the mechanism requirement of the electrochemical sensors. We also revealed the benefit of the composite on the electrochemical effective area using the Randles−Sevcik equation in the Supporting Information (Supplement S3). By fitting the results of Figure S3a−d, the effective areas of the bare

https://doi.org/10.1021/acsami.2c09446
ACS Appl. Mater. Interfaces 2022, 14, 40569−40578

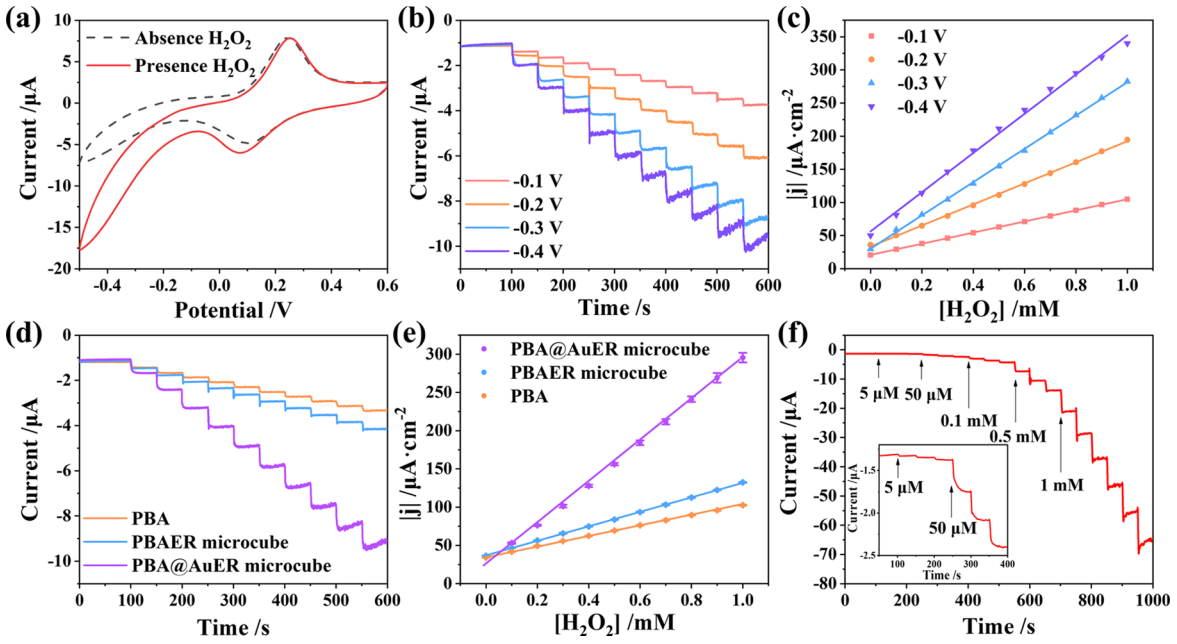

Figure 5. (a) CV results of the PBA@AuER microcube-modified gold electrode in the absence and presence of H_2O_2 in 0.05 M PBS at a scan rate of 50 mV/s. (b) *I*−*t* results of the PBA@AuER microcube to H_2O_2 in 0.05 M PBS at different working potentials. (c) Calibration curves of different working potentials according to the *I*−*t* results. (d) *I*−*t* results of the PBA, PBAER microcube, and PBA@AuER microcube to H_2O_2 under −0.3 V in 0.05 M PBS. (e) Calibration curves of PBA, PBAER, and PBA@AuER under −0.3 V according to the *I*−*t* results. (f) Linear range of the PBA@AuER composite for H_2O_2 detection under −0.3 V in 0.05 M PBS. Inset showing magnifications of the *I*−*t* result from 50 to 400 s.

electrode, PBA, PBAER microcubes, and PBA@AuER microcube-modified electrodes were calculated to be 0.031, 0.040, 0.048, and 0.051 cm^2, respectively (Figure 4h). Consequently, we can conclude that the formation of the edge-rich microcube compared to the original microcube enables the enhancement of the effective area by 19.8% because of the additional created edges on each crystal surface; moreover, the introduction of AuNP layers can further increase 7.0% area.

2.3. Sensing Performance of the PBA@AuER Microcube-Based Film to H_2O_2. In our previous work, H_2O_2 is the final product of glucose oxidase (GOD) enzymatic reactions.[28] Hence, the composite based electrode was applied to test its performance on the H_2O_2 detection. After the addition of 0.5 mM H_2O_2, the oxidation current was decreased, and the reduction current was greatly increased, which indicated a reduction behavior to H_2O_2 (Figure 5a). Evidently, the current change varied significantly when the potential was below −0.1 V. Therefore, we carefully studied the sensing performance of this composite at different operation potentials from −0.1 to −0.4 V. With continuous injection of 0.1 mM H_2O_2, all potentials can produce successive current steps (Figure 5b). Meanwhile, a more negative potential aroused a higher response current. As fitted in Figure 5c, the sensitivities of the PBA@AuER microcubes were 84.08, 158.96, 261.19, and 296.02 μA·mM^{-1}·cm^{-2} for −0.1, −0.2, −0.3, and −0.4 V, respectively. Although there was a higher current response at −0.4 V, the linear range at this potential was especially narrow. Consequently, −0.3 V was selected as the optimum parameter to balance both the above performances. Furthermore, under this potential, the performances of the PBA, PBAER microcube, and PBA@AuER microcube were tested to compare their electrocatalytic abilities. As shown in the *I*−*t* results (Figure 5d), It can be observed that the composite was of a superior current response when adding the same concentration of H_2O_2. The sensitivities of the above three materials were linearly fitted as 68 and 95 and 271 μA·mM^{-1}·cm^{-2}, respectively (Figure 5e). The performance of the PBA@AuER microcube was nearly three times as high as that of the PBAER microcube. As above demonstrated, the composite possessed a superior effective area, conductivity, and electrocatalysis, which had provided a synergetic promotion to the H_2O_2 reduction. Moreover, this material enabled us to fulfill its detection in an ultrawide concentration range from 5 μM to 5.5 mM with a lowest detection limit of 1.5 μM, confirming its remarkable electron transfer ability and electrocatalytic efficiency for promoting target diffusion (Figure 5f).

2.4. Screen Printing of the PBA@AuER Microcube-Based Microchip. Considering the practical industrial application, different from the clinical biosensor, the desired fermentation biosensor is required to possess ultrahigh reusability to satisfy the monitoring of the long-period fermentation reaction; we proposed a screen-printed method to deliver a biosensor microchip using PBA@AuER microcubes as the printing ink.[29] In this route, the obtained composite was mixed with carbon paste to increase its viscosity and mobility to prepare a satisfactory printing ink. As shown in Figure 6a, this ink was sufficiently smooth to write continuous words using a Chinese brush, confirming its uniform mixing. According to the XRD results in Figure 6b, the described mixing process produced few changes in the crystal structures of PBA and AuNPs to maintain their typical face peaks. In addition, the Fourier transform infrared (FTIR) maps (Figure 6c) present three clear transmittance peaks of the PBA@AuER microcubes at 1606, 2188, and 3435 cm^{-2}, corresponding to −COOH, −C≡N−, and −OH, respectively. The −OH and −COOH groups in the composite were derived from the water molecules occupying the lattice pores of PBA to induce the stretching and bending vibrations, whereas the −C≡N− originated from the coordination unit of Cu−N≡C−Co in PBA.[30] The composite ink, carbon, and Ag/AgCl inks were

https://doi.org/10.1021/acsami.2c09446
ACS Appl. Mater. Interfaces 2022, 14, 40569−40578

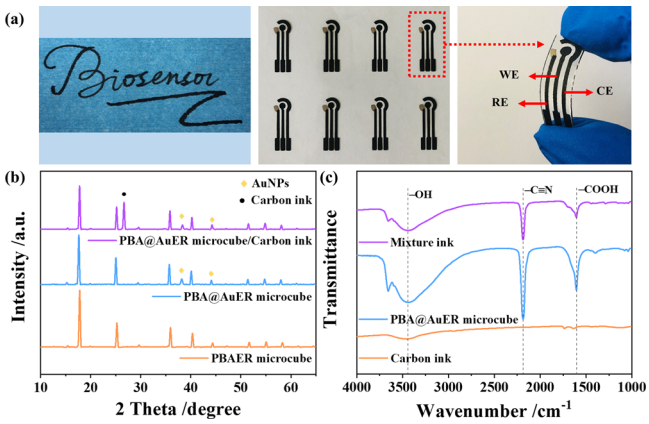

Figure 6. (a) Preparation of flexible SPM with conductive carbon ink. (b) XRD patterns of the PBAER microcube, PBA@AuER microcube, and PBA@AuER microcube mixed carbon ink. (c) FTIR spectra of carbon ink, PBA@AuER microcube, and PBA@AuER microcube mixed carbon ink.

directly applied to print the working, counter, and reference electrodes, respectively. The as-prepared microchip was flexible and exhibited no damage to the electrodes during bending owing to the good ductility of the ink and the performances of the 0.5 mm PET. The working electrode containing the −COOH group in the composite ink is beneficial for further loading of enzymes. Due to the $-NH_2$ group present in the general enzymes, the abundant −COOH groups are beneficial for establishing $-CONH_2$ bonds for the enzyme immobilization.[31] Moreover, glutaraldehyde can react with free amino groups in protein molecules to achieve cross-linking effect. These two steps can provide good enzyme immobilization on the surface of the electrode, achieving better usage stability.

In terms of the detection principle, sucrose is a disaccharide composed of one glucose and fructose molecule; therefore, a multiple-enzyme strategy using invertase (INV), mutarotase (MUT), and glucose oxidase (GOD) can be designed to decompose sucrose to glucose for recognition. This reaction mechanism can be described as following equations:

$$\text{Sucrose} + H_2O \xrightarrow{\text{INV}} \text{D-Fructose} + \alpha\text{-D-Glucose} \quad (3)$$

$$\alpha\text{-D-Glucose} \xrightarrow{\text{MUT}} \beta\text{-D-Glucose} \quad (4)$$

$$\beta\text{-D-Glucose} + O_2 \xrightarrow{\text{GOD}} \text{D-Glucono-1, 5-lactone} + H_2O_2 \quad (5)$$

$$H_2O_2 \rightarrow O_2 + 2e^- + 2H^+ \quad (6)$$

Sucrose can be decomposed into D-fructose and α-D-glucose under the hydrolysis of INV. Since GOD only undergoes enzymatic reaction against ß-D-glucose, we introduce MUT to realize the conversion from α-D-glucose to β-D-glucose. Under the combined action of the multiple-enzyme system, the final product H_2O_2 is generated for signal detection.

2.5. Biosensing Performance of the Microchip. According to our design, INV, MUT, and GOD were immobilized layer-by-layer on the microchip to realize the recognition of sucrose. Notably, owing to the application of GOD, the as-prepared enzymatic microchip was also able to respond to glucose. Thus, we tested the biosensing performance of this microchip using sucrose and glucose as the targets. As observed in Figure 7a, both additions of sucrose and glucose can give rise to the stable current steps under a work

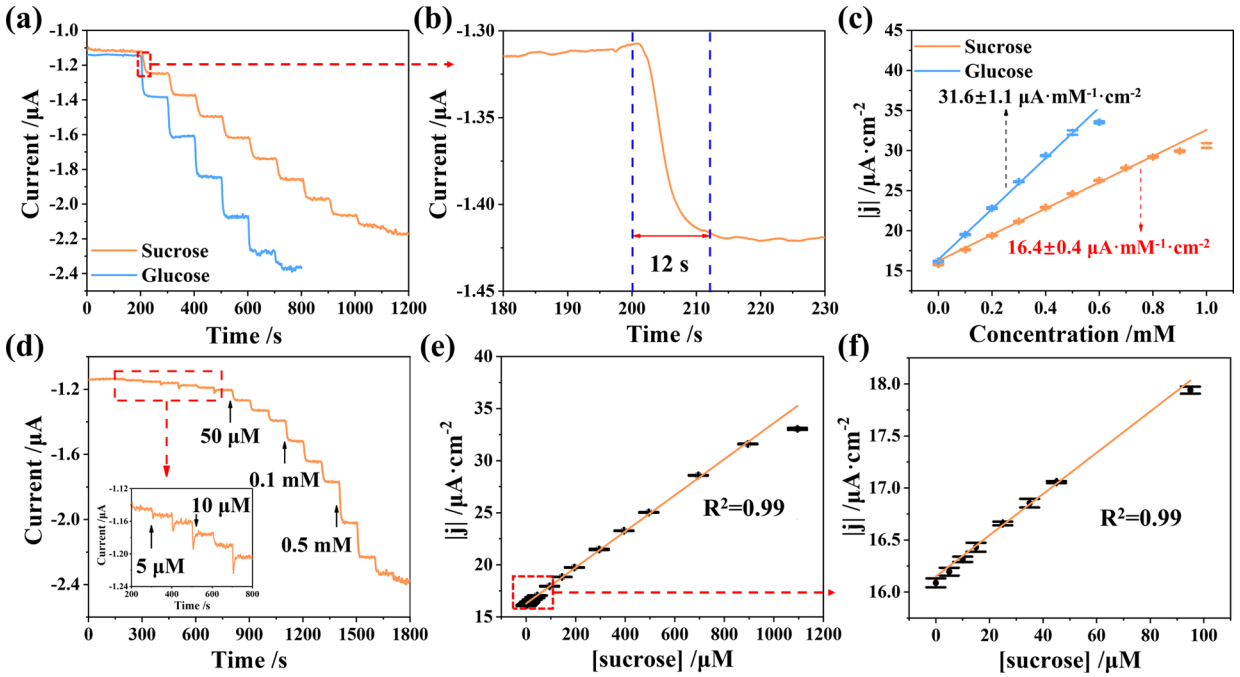

Figure 7. (a) *I*−*t* results of the PBA@AuER microcubes/SPM for sucrose and glucose at −0.3 V in 0.05 M PBS with 0.1 mM sucrose and 0.1 mM glucose. (b) Response time of PBA@AuER microcubes/SPM for sucrose detection. (c) Calibration lines of the relevance between response current and the concentration of glucose or sucrose. (d) *I*−*t* image when continuously adding the sucrose from low to high concentrations, inset showing magnifications of the *I*−*t* result from 200 to 800 s. (e) Linear calibration of the PBA@AuER microcubes/SPM at −0.3 V in 0.05 M PBS. (f) Magnifications of the linear calibration at low concentrations.

https://doi.org/10.1021/acsami.2c09446
ACS Appl. Mater. Interfaces 2022, 14, 40569−40578

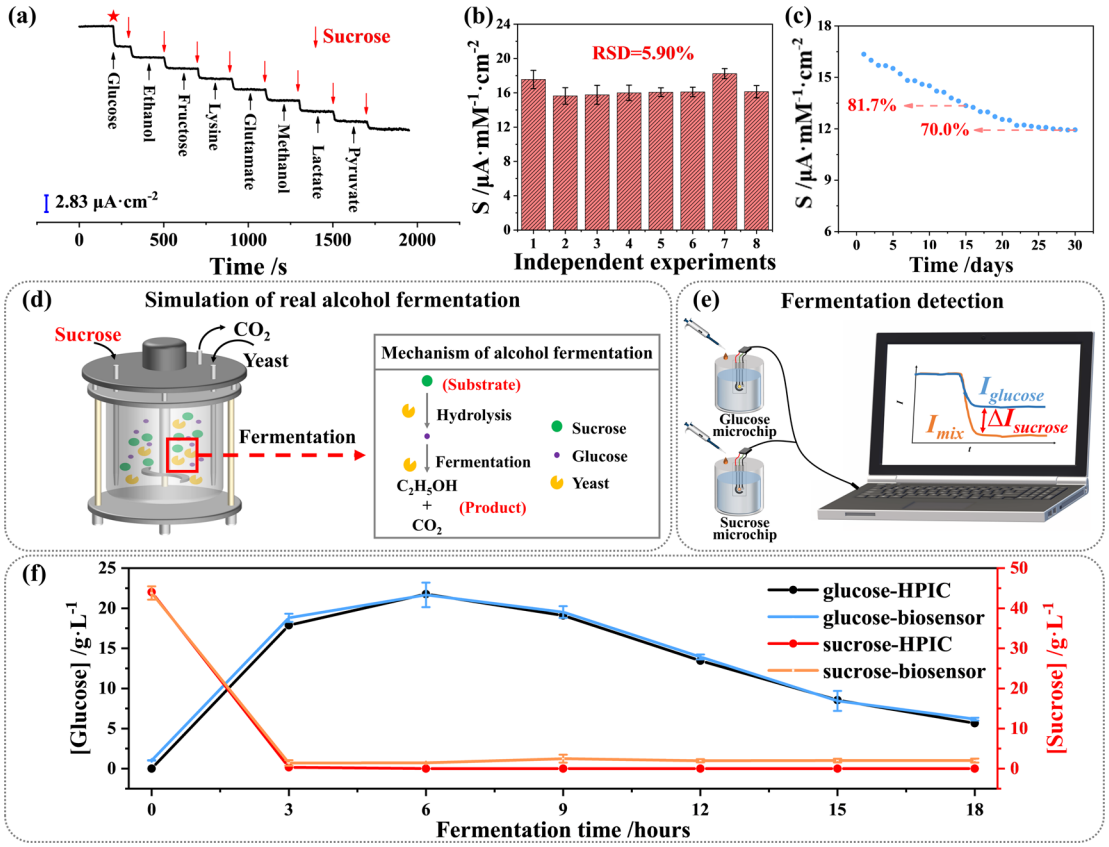

Figure 8. (a) Anti-interference ability of the as-prepared S-chip to glucose, ethanol, fructose, glutamate, lysine, methanol, lactate, and pyruvate. The addition concentrations of interfering substances and sucrose were 0.1 mM. (b) Sensitivities of the prepared 8 S-chips through independent tests. (c) Monitoring of the sensitivity of a single S-chip during the repetitive usage in 30 days. (d) Simulation of real alcohol fermentation. (e) Schematic diagram of real fermentation detection. (f) Analysis results for sucrose and glucose in real fermentation broth.

potential of −0.3 V, which is the same as that of the electrocatalytic potential of H_2O_2. Although three enzymatic reactions were employed, the response time was only 12 s (Figure 7b), demonstrating the fast electrocatalytic and electron transfer abilities of the composite. Through the linear fittings of the response current with the target concentration (Figure 7c), the sensitivities of the microchip were 31.7 ± 1.1 and 16.4 ± 0.4 $\mu A \cdot mM^{-1} \cdot cm^{-2}$ for glucose and sucrose, respectively. To characterize the linear detection range, different sucrose concentrations from low to high (5 μM to 0.5 mM) were successively added to examine the linear relationship (Figure 7d). According to the results in Figure 7e, the response current did well follow the linear equation $j = 0.017C_{sucrose} + 16.3$ under a wide concentration range from 5 μM to 1.3 mM with an limit of detection (LOD) of 5 μM ($S/N = 3$) (the details of the calculation of the LOD of sucrose are shown in the Supporting Information (Supplement S4)). Magnifications of the linear calibration at low concentrations are shown in Figure 7f. By performance comparison of various nanomaterial-based sucrose biosensors, it is observed that the as-prepared sucrose microchip can achieve higher sensitivity and faster detection under the condition of coexistence of multiple components while considering a lower working potential. (The details of comparison of various sucrose biosensors are shown in the Supporting Information (Supplement S5)).

2.6. Practical Test in the Real Fermentation Process. Anti-interference ability, reproducibility, and stability are essential parameters in real fermentation detection. After the injection of the common fermented substances, there was no significant change in current, indicating the excellent anti-interference ability of the as-prepared biosensor microchip (Figure 8a). The RSD of sensitivity derived from eight microchips was 5.90%, indicating the excellent performance of repeatability in the large-scale production (Figure 8b). Moreover, a single microchip was randomly selected to detect sucrose 10 times per day for 30 days to study its reusability, and the sensitivity on the 30th day can still remain at 70.0%, illustrating the excellent reusability of the microchip (Figure 8c). The details of anti-interference ability, reproducibility, and stability of the microchip can be obtained from the Supporting Information (Supplement S6). In the fermentation process of wine using sucrose as a carbon source, glucose and sucrose are often mixed in the fermentation broth because of the hydrolysis of sucrose to produce glucose, which is fermented by yeast to produce alcohol.[32] In this case, the detection signals of glucose and sucrose will be simultaneously produced to mix together, resulting in the great challenge of distinguishing each concentration of glucose and sucrose. To address this issue, we propose an analytical strategy focused on a binary mixture system. This analysis strategy involves calculating the current value of sucrose in the binary component using the current differential method and thereafter substituting this current value into the fitting formula to obtain the sucrose concentration. The details of the binary-component calculation model are provided in the Supporting Information (Supplement S8).

https://doi.org/10.1021/acsami.2c09446
ACS Appl. Mater. Interfaces 2022, 14, 40569−40578

We used a real fermentation reaction to examine the accuracy of the as-prepared microchip and designed an analytical strategy. In this experiment, 50 g/L sucrose and 2 g of yeast were added to a small fermenter to maintain a constant temperature of 30 °C (Figure 8d). During fermentation, several samples were collected every 3 h for detection using microchips and high-performance ion chromatography (HPIC). As shown in Figure 8e, by following the proposed analytical strategy for a binary mixture system (Figures S6 and S7), the concentration fluctuations of sucrose and glucose with fermentation time were fitted, as shown in Figure 8f. It was found that the sucrose concentration in the fermentation broth gradually decreased with an increase in reaction time but subsequently decreased to a steady level in the later stage. Moreover, the glucose concentration increased with the hydrolysis of sucrose in the early stage; thereafter, the concentration decreased under the action of yeast fermentation, satisfying the normal fermentation process. In particular, the detected concentrations of sucrose and glucose using the microchips are in agreement with results tested by HPIC with RSDs of 6.83 and 5.11%, demonstrating that our fabricated biosensing microchips and delivered analytical strategy are capable of monitoring the substrate concentrations in the practical fermentation.

3. CONCLUSIONS

In conclusion, to achieve sucrose monitoring in the fermentation process, a highly sensitive and fast biosensor microchip was fabricated by establishing a PBA@AuER microcube. This material has been confirmed to induce a synergic effect of both high electrocatalysis and conductivity on three enzymatic reactions, which are designed to precisely recognize sucrose within only 12 s. The as-prepared microchip exhibited outstanding reusability, accuracy, and anti-interference for long-term monitoring of sucrose fluctuations in a real alcohol fermentation process. This stable and fast-response biosensor is beneficial for instrument transfer and provides an advanced technique for the real-time control of microbial metabolism during the fermentation process, thereby increasing yield and decreasing waste.

4. EXPERIMENTAL SECTION

4.1. Materials and Apparatus. Potassium hexacyanocobaltate-(III), 98%, ($K_3[Co(CN)_6]$) was obtained from J&K Scientific. Copper(II) chloride dihydrate ($CuCl_2{\cdot}2H_2O$), ascorbic acid (AA), and sodium citrate dihydrate ($Na_3C_6H_5O_7{\cdot}2H_2O$) were acquired from Aladdin, China. Dipotassium hydrogen phosphate (K_2HPO_4), potassium dihydrogen phosphate (KH_2PO_4), glutaraldehyde 25% (vol/vol), absolute ethanol, and potassium chloride (KCl) were purchased from Shanghai Lingfeng Chemical Reagent Co. Ltd. (China). GOD and D-glucose were obtained from Sigma-Aldrich. INV and MUT were purchased from Shanghai Yuanye Biotechnology Co. Ltd. D-Fructose, lactate, glutamate, pyruvate, lysine, methanol, and sucrose were provided by Shanghai Macklin Biochemical Co. Ltd. Chloroauric acid ($HAuCl_4$, ≥99%) was provided by Sinopharm Chemical Reagent Co. Ltd. (China). Conductive carbon and silver chloride inks were acquired from Henkel-Loctite Co. Ltd. The as-prepared PBS is composed of dipotassium hydrogen phosphate (K_2HPO_4), potassium dihydrogen phosphate (KH_2PO_4), and potassium chloride (KCl). Their respective concentrations are 0.04, 0.06, and 0.1 M. All chemicals used in this study were directly used without further purification. All aqueous solutions were prepared using deionized (DI) water (≥18.2 MΩ, Smart2Pure 6, Thermo Fisher Scientific, USA).

FESEM (Hitachi, ModelS-4800II, Japan) was used to examine the micromorphology. XRD was performed using an X-ray diffractometer (D/MAX 2500 V/PC) with a Cu-Kα line (0.15419 nm). XPS and spectroscopy of the samples were performed with X-ray photoelectron spectrometry (Thermo, ESCALAB 250) and FTIR (Thermo Electron, Nicolet 8700) instruments, respectively. TEM was performed using a JEOL JEM-2010 UHR instrument. SECM was performed using a CHI920D (Shanghai Chenhua Instrument Co., Ltd., China). Screen-printed microchips (SPMs) were fabricated using a 245 DEK screen-printing machine (Weymouth, United Kingdom). A NORDSON EFD three-dimensional dotting-enzyme machine (JR-V2303 MI, Taiwan) was used to immobilize enzyme solutions on the surface of the working electrode. All electrochemical measurements, including CV, chronoamperometry (I–t), and EIS, were performed with an electrochemical workstation (CHI 660E, Shanghai Chenhua Instrument Co., Ltd., China). HPIC (Thermo Scientific ICS-5000 HPIC) was used to detect sucrose and glucose concentrations. The chromatographic system adopts a Thermo ICS5000 (Dionex, Thermo Scientific, Waltham, US) ion chromatographic system and CarboPac PA10 (250 × 3.0 mm) liquid chromatographic column, the mobile phase is A: H_2O and B:100 mM NaOH, the detector is an electrochemical detector, the injection volume is 5 μL, the flow rate is 0.5 mL/min, and the column temperature is 30 °C. In order to construct a H_2O_2 sensor on a gold disk electrode, 20 mg of powder (PBA, PBAER microcubes, and PBA@AuER microcubes) was mixed in 10 mL of DI water and stirred homogeneously. Then, 2.5 μL of the mixed suspension was dropped on the gold disk electrode and dried completely. The prepared H_2O_2 sensors were stored at 4–8 °C in a refrigerator for 12 h to achieve a curing effect. EIS was applied to investigate the resistance of electron transfer (R_{ct}) in solution. EIS characterization was carried out in the presence of 5 mM $[Fe(CN)_6]^{3-/4-}$solution containing 0.1 M KCl, and the frequency ranges were from 0.01 Hz to 10 MHz. The effective area was tested in the solution of 10 mM $K_3[Fe(CN)_6]$ and 3 M KCl. The I–t tests were carried out at −0.3 V in 0.05 M PBS. In all CV tests, the scan rate and sampling frequency were 0.1 V/s and 0.001 V, respectively. All experiments in the electrochemical detection section were carried out in 0.05 M PBS, and these experiments were performed at room temperature. To further explore the LOD of sucrose, a signal-to-noise ratio benchmark was determined (S/N = 3). During the experiment of real fermentation, 50 g/L sucrose and 2 g of yeast were added into a 500 mL fermenter to maintain a constant temperature of 30 °C. During the fermentation detection process, several samples were collected every 3 h for detections using the microchips and HPIC.

4.2. Synthesis of the PBA@AuER Composite. For the one-step facile synthesis of PBAER crystals, two solutions were prepared: solution A (100 mL): 30 mM $K_3[Co(CN)_6]$ and solution B (100 mL): 30 mM $CuCl_2{\cdot}2H_2O$ + 45 mM $Na_3C_6H_5O_7{\cdot}2H_2O$. Solution B was stirred for 30 min in advance to achieve full complexation. Next, solution A was directly poured into solution B and thereafter stood for 10 min. After the reaction was complete, wet PBAER microcubes were obtained by adding DI water to wash and centrifuge three times at a speed of 8000 rpm.

Subsequently, we continued to disperse the wet PBAER microcubes in a beaker containing 150 mL of DI water and stirred them for 10 min in a 35 °C constant-temperature water bath. Next, 50 mL of 60 mM $CuCl_2{\cdot}2H_2O$ solution was added to the suspension and the PBAER crystal surface uniformly scattered positive ions through magnetic stirring for 12 h. Then, 10 mL of 5 mM $HAuCl_4$ was added to the beaker, and $[AuCl_4]^-$ was loaded on the surface of the PBAER owing to electrostatic attraction. We used 10 mM AA to reduce Au^{3+} with an injection rate of 300 μL/min. After the complete microspeed injection of AA, the color of the suspension solution converts from blue to purple significantly. Finally, PBA@AuER microcubes were obtained by adding DI water and ethanol to wash and centrifuge three times at a speed of 8000 rpm. The final product was dried at 60 °C and stored at 4 °C.

4.3. Construction of the Sucrose Biosensor Based on Screen-Printed Microchips. Two three-electrode SPMs were

https://doi.org/10.1021/acsami.2c09446
ACS Appl. Mater. Interfaces 2022, 14, 40569–40578

prepared using a screen printer. The working electrode material was obtained by uniformly mixing PBA@AuER microcubes and carbon ink at a mass ratio of 1:9, using a silver chloride slurry as the reference electrode. The counter electrode and connected portion were composed of carbon ink. The 0.5 mm PET was used as the printed substrate to meet the requirements of flexibility.

Sucrose microchip (S-chip): 5 mg of GOD was dissolved in 495 μL of PBS, and thereafter, 5 μL of 25% glutaraldehyde solution was added to the above PBS and mixed well with a shaker to prepare the GOD solution. The INV solution was prepared using the same method. The MUT solution was prepared by diluting the enzyme solution from 28 to 1 U/μL by adding PBS. Subsequently, we followed the order of INV, MUT, and GOD to drip 4, 2, and 4 μL of enzyme solutions layer-by-layer on the surface of the working electrode of the S-chip. The prepared S-chips were stored at 4−8 °C in a refrigerator.

Glucose microchip (G-chip): 5 μL of the GOD solution prepared in the above steps was taken out and dripped on the surface of the electrode. After drying at room temperature, it was stored at 4−8 °C in a refrigerator.

The S-chip and G-chip work simultaneously during fermentation through a novel analytical strategy for the binary mixture substrate system. Moreover, we achieve this goal by running two electrochemical workstations simultaneously.

■ ASSOCIATED CONTENT

Supporting Information

The Supporting Information is available free of charge at https://pubs.acs.org/doi/10.1021/acsami.2c09446.

FESEM images; XPS spectra; CV diagrams; chronoamperometry diagram; performance comparison; anti−interference ability, reproducibility, and stability of the microchip; stability experiment; and analytical strategy (PDF)

■ AUTHOR INFORMATION

Corresponding Author

Zhenyu Chu − *State Key Laboratory of Materials-Oriented Chemical Engineering, College of Chemical Engineering, Nanjing Tech University, Nanjing 211816, P. R. China;* orcid.org/0000-0001-6337-3101; Phone: +86 25-8317-2173; Email: zychu@njtech.edu.cn

Authors

Ke Zhang − *State Key Laboratory of Materials-Oriented Chemical Engineering, College of Chemical Engineering, Nanjing Tech University, Nanjing 211816, P. R. China*

Meiqi Wang − *State Key Laboratory of Materials-Oriented Chemical Engineering, College of Chemical Engineering, Nanjing Tech University, Nanjing 211816, P. R. China*

Tao Liu − *State Key Laboratory of Materials-Oriented Chemical Engineering, College of Chemical Engineering, Nanjing Tech University, Nanjing 211816, P. R. China*

Wanqin Jin − *State Key Laboratory of Materials-Oriented Chemical Engineering, College of Chemical Engineering, Nanjing Tech University, Nanjing 211816, P. R. China;* orcid.org/0000-0001-8103-4883

Complete contact information is available at: https://pubs.acs.org/10.1021/acsami.2c09446

Author Contributions

K.Z.: experimental executor, experimental analysis, discussion, and writing—original draft. M.W.: discussion and writing—original draft. T.L.: experimental analysis and discussion. Z.C.: project administration, supervision, experimental analysis, funding acquisition, validation, writing—original draft, and writing—review and editing. W.J.: project administration, supervision, funding acquisition, and writing—review and editing.

Notes

The authors declare no competing financial interest.

■ ACKNOWLEDGMENTS

This work was financially supported by the National Key R&D Program of China (Grant No. 2021YFC2103300), the National Natural Science Foundation of China (Nos. 21727818 and 22078148), and project funded by the Priority Academic Program Development of Jiangsu Higher Education Institutions (PAPD).

■ REFERENCES

(1) Sgobba, E.; Stumpf, A. K.; Vortmann, M.; Jagmann, N.; Krehenbrink, M.; Dirks-Hofmeister, M. E.; Moerschbacher, B.; Philipp, B.; Wendisch, V. F. Synthetic Escherichia Coli−Corynebacterium Glutamicum Consortia for L−lysine Production from Starch and Sucrose. *Bioresour. Technol.* **2018**, *260*, 302−310.

(2) Breisha, G. Z. Production of 16% Ethanol from 35% Sucrose. *Biomass Bioenergy* **2010**, *34*, 1243−1249.

(3) Li, S.; Chen, D. Q.; Ji, L.; Sun, S.; Jin, Z.; Jin, Z. L.; Sun, H. W.; Zeng, H.; Zhang, W. J.; Lu, D. S.; Luo, P.; Zhao, A. N.; Luo, J.; Zou, Q. M.; Li, H. B. Development of Different Methods for Preparing Acinetobacter Baumannii Outer Membrane Vesicles Vaccine: Impact of Preparation Method on Protective Efficacy. *Front. Immunol.* **2020**, *11*, 1069.

(4) Saborido-Fiano, R.; Martinon-Torres, N.; Crujeiras-Martinez, V.; Couce, M. L.; Leis, R. Reply Letter to "Safety of SARS-Cov-2 Vaccines Administration for Adult Patients with Hereditary Fructose Intolerance. *Hum. Vaccines Immunother.* **2021**, *17*, 4115−4116.

(5) Moghimi, S. M. Allergic Reactions and Anaphylaxis to Lipid Nanoparticle−based COVID−19 Vaccines. *Mol. Ther.* **2021**, *29*, 898−900.

(6) Zhao, P. X.; Hou, X. C.; Yan, J. Y.; Du, S.; Xue, Y. R.; Li, W. Q.; Xiang, G. Y.; Dong, Y. Z. Long−Term Storage of Lipid−like Nanoparticles for mRNA Delivery. *Bioact. Mater.* **2020**, *5*, 358−363.

(7) Wimonsong, P.; Nitisoravut, R.; Llorca, J. Application of Fe−Zn−Mg−Al−O Hydrotalcites supported Au as Active Nano−catalyst for Fermentative Hydrogen Production. *Chem. Eng. J.* **2014**, *250*, 148−154.

(8) Reddy, L. V.; Park, J.; Wee, Y. Homofermentative Production of Optically Pure L−lactic acid from Sucrose and Mixed Sugars by Batch Fermentation of Enterococcus Faecalis RKY1. *Biotechnol. Bioprocess Eng.* **2015**, *20*, 1099−1105.

(9) Malbaša, R.; Lončar, E.; Djurić, M.; Došenović, I. Effect of Sucrose Concentration on the Products of Kombucha Fermentation on Molasses. *Food Chem.* **2018**, *108*, 926−932.

(10) Khaliq, N.; Rasheed, M. A.; Khan, M.; Maqbool, M.; Ahmad, M.; Karim, S.; Nisar, A.; Schmuki, P.; Cho, S. O.; Ali, G. Voltage−Switchable Biosensor with Gold Nanoparticles on TiO_2 Nanotubes Decorated with CdS Quantum Dots for the Detection of Cholesterol and H_2O_2. *ACS Appl. Mater. Interfaces* **2021**, *13*, 3653−3668.

(11) Zhang, S. J.; Xie, Y.; Feng, J. Y.; Chu, Z. Y.; Jin, W. Q. Screen-printing of Nanocube-based Flexible Microchips for the Precise Biosensing of Ethanol During Fermentation. *AIChE J.* **2021**, *67*, No. e17142.

(12) Feng, J.; Liu, Y.; Shan, Y.; Xie, Y.; Chu, Z.; Jin, W. In−situ Growth of Cu@CuFe Prussian blue based Core−shell Nanowires for Non−enzymatic Electrochemical Determination of Ascorbic acid with high sensitivity and reusability. *J. Electroanal. Chem.* **2021**, *900*, No. 115718.

(13) Maduraiveeran, G.; Sasidharan, M.; Ganesan, V. Electrochemical Sensor and Biosensor platforms based on Advanced

Nanomaterials for Biological and Biomedical Applications. *Biosens. Bioelectron.* **2018**, *103*, 113−129.
(14) Tian, L.; Zhang, Y.; Wang, L. B.; Geng, Q. J.; Liu, D. X.; Duan, L. L.; Wang, Y. H.; Cui, J. S. Ratiometric Dual Signal−Enhancing−Based Electrochemical Biosensor for Ultrasensitive Kanamycin Detection. *ACS Appl. Mater. Interfaces* **2021**, *12*, 52713−52720.
(15) Soto, R. T.; Schofield, J. B.; Walter, S. E.; Malone-Povolny, M. J.; Schoenfisch, M. H. Design Considerations for Silica−Particle−Doped Nitric−Oxide−Releasing Polyurethane Glucose Biosensor Membranes. *ACS Sens.* **2017**, *2*, 140−150.
(16) Chu, Z.; Zhang, W.; You, Q.; Yao, X.; Liu, T.; Liu, G.; Zhang, G. R.; Gu, X.; Ma, Z.; Jin, W. A Separation-Sensing Membrane Performing Precise Real-Time Serum Analysis During Blood Drawing. *Angew. Chem., Int. Ed.* **2020**, *59*, 18701−18708.
(17) Liu, P.; Qian, X. Q.; Li, X. M.; Fan, L.; Li, X. Y.; Cui, D. X.; Yan, Y. R. Enzyme−Free Electrochemical Biosensor Based on Localized DNA Cascade Displacement Reaction and Versatile DNA Nanosheets for Ultrasensitive Detection of Exosomal MicroRNA. *ACS Appl. Mater. Interfaces* **2020**, *12*, 45648−45656.
(18) Barber, E.; Houghton, M. J.; Williamson, G. Flavonoids as Human Intestinal alpha−Glucosidase Inhibitors. *Foods.* **2021**, *10*, 1939.
(19) Mieres-Castro, D.; Theoduloz, C.; Sus, N.; Burgos-Edwards, A.; Schmeda-Hirschmann, G.; Frank, J.; Jimenez-Aspee, F. Iridoids and Polyphenols from Chilean Gaultheria spp. berries Decrease the Glucose uptake in Caco-2 cells after Simulated Gastrointestinal Digestion. *Food Chem.* **2022**, *369*, No. 130940.
(20) Chu, Z. Y.; Liu, Y.; Jin, W. Q. Recent Progress in Prussian Blue Films: Methods used to Control Regular Nanostructures for Electrochemical Biosensing Applications. *Biosens. Bioelectron.* **2017**, *96*, 17−25.
(21) Chu, Z. Y.; Peng, J. M.; Jin, W. Q. Advanced Nanomaterial Inks for Screen−printed Chemical Sensors. *Sens. Actuators, B* **2017**, *243*, 919−926.
(22) Xia, X. H.; Liu, L.; Li, X. H.; Gao, S. S.; Yang, T. Y. Highly Efficient Electrocatalytic Hydrogen Evolution over Edge-modified Phosphorene Quantum dot/Prussian blue Skeleton Structure. *J. Catal.* **2019**, *374*, 401−408.
(23) Feng, J. J.; Zhu, W.; Zhang, Z. W.; Cao, L. L.; Yu, Y.; Deng, Y. Enhanced Electrical Transport Properties via Defect Control for Screen−Printed Bi_2Te_3 Films over a Wide Temperature Range. *ACS Appl. Mater. Interfaces* **2020**, *12*, 16630−16638.
(24) Wang, Y.; Shi, F.; Yang, Y.; Cai, W. Carbon Supported Pd−Ni−P Nanoalloy as an Efficient Catalyst for Ethanol Electro−oxidation in Alkaline Media. *J. Power Sources* **2013**, *243*, 369−373.
(25) Deng, Z.; Jiang, H.; Hu, Y.; Li, C.; Liu, Y.; Liu, H. Nanospace-confined Synthesis of Coconut-like SnS/C Nanospheres for High-rate and Stable Lithium-ion Batteries. *AIChE J.* **2018**, *64*, 1965−1974.
(26) Chong, S.; Yang, J.; Sun, L.; Guo, S.; Liu, Y.; Liu, H. Potassium Nickel Iron Hexacyanoferrate as Ultra−Long−Life Cathode Material for Potassium−Ion Batteries with High Energy Density. *ACS Nano* **2020**, *14*, 9807−9818.
(27) Liu, T.; Zhao, Q.; Xie, Y.; Jiang, D.; Chu, Z.; Jin, W. In situ Fabrication of Aloe-like Au−ZnO Micro/nanoarrays for Ultrasensitive Biosensing of Catechol. *Biosens. Bioelectron.* **2020**, *156*, No. 112145.
(28) Yang, P. Q.; Pang, J.; Hu, F. H.; Peng, J. M.; Jiang, D. F.; Chu, Z. Y.; Jin, W. Q. An Ultrasensitive Biosensing Flexible Chip using a Novel Silver@Prussian blue core−shell Nanocube Composite. *Sens. Actuators, B* **2018**, *276*, 31−41.
(29) Zhu, S. S.; Tian, J. Q.; Zhang, J. J.; Gao, C. X.; Liu, X. Z. Improving the Interfacial Contact of Screen−Printed Carbon Electrodes for Perovskite Solar Cells. *ACS Appl. Mater. Interfaces* **2021**, *4*, 5554−5559.
(30) Karikalan, N.; Velmurugan, M.; Chen, S. M.; Chelladurai, K. A Copper Hexacyanocobaltate Nanocubes based Dopamine Sensor in the Presence of Ascorbic acid. *RSC Adv.* **2016**, *6*, 48523−48529.
(31) Hu, F.; Liu, T.; Pang, J.; Chu, Z.; Jin, W. Facile Preparation of Porous Co_3O_4 Nanocubes for Directly Screen−printing an Ultra-sensitive Glutamate Biosensor Microchip. *Sens. Actuators, B* **2020**, *306*, No. 127587.
(32) Rzechonek, D. A.; Dobrowolski, A.; Rymowicz, W.; Mironczuk, A. M. Recent Advances in Biological Production of Erythritol. *Crit. Rev. Biotechnol.* **2018**, *38*, 620−633.

https://doi.org/10.1021/acsami.2c09446
ACS Appl. Mater. Interfaces 2022, 14, 40569−40578